RSC Advances

PAPER

Cite this: *RSC Adv.*, 2025, **15**, 13857

Polydopamine-functionalized acellular fish scale scaffolds for accelerated bone tissue regeneration†

Shilong Su, [ab] Ruideng Wang, [ab] Jinwu Bai,[ab] Shan Gao,[ab] Rubing Zhou[c] and Fang Zhou *[ab]

Received 18th March 2025
Accepted 24th April 2025

DOI: 10.1039/d5ra01932j

rsc.li/rsc-advances

The complex microenvironment changes in the bone defect site are the main reason for its refractory treatment, including the significant increase in the level of reactive oxygen species (ROS) and inflammatory dysregulation. There is an urgent need to develop some bioactive materials that can regulate the microenvironment and promote bone regeneration. This study proposed a new strategy for designing bone tissue engineering scaffolds based on fish scales and developed a polydopamine-functionalized acellular fish scale scaffold (PDA-AFS). The results showed that PDA-AFS had excellent mechanical properties, special three-dimensional surface topography, and biodegradability. *In vitro* results showed that PDA-AFS had good biocompatibility and cell adhesion ability, could effectively reduce ROS levels, and had immunomodulatory activity. More importantly, PDA-AFS can enhance osteogenic differentiation of bone marrow mesenchymal stem cells and promote endogenous bone regeneration in critical-sized calvarial bone defects. In addition, transcriptome analysis also provided clues to its possible osteogenic mechanism. Overall, we provide a new strategy for designing bone tissue engineering scaffolds based on fish scales for bone regeneration treatment of bone defects.

1. Introduction

Bone defects caused by various reasons such as infection, tumor, and trauma are common diseases in clinical practice.[1] The complex microenvironment changes in the bone defect site are the main reason for its refractory treatment, including the significant increase in the level of reactive oxygen species (ROS) and inflammatory dysregulation.[2,3] High levels of ROS can cause cell damage and disrupt normal signaling pathways, causing the differentiation of bone marrow mesenchymal stem cells (BMSCs) to shift from osteogenic to adipogenic phenotypes, ultimately inhibiting bone healing.[4] Bone regeneration begins with an inflammatory response, accompanied by a dynamic regulation of the inflammatory microenvironment.[5] Macrophages are one of the most important immune cells, and they polarize to the M1 phenotype in the early stage of bone regeneration, giving these cells phagocytic and scavenging properties. Subsequently, anti-inflammatory M2 phenotype macrophages dominate within the first three days.[6] Studies have found that M2 phenotype macrophages can not only secrete anti-inflammatory factors such as interleukin-10 (IL-10), effectively alleviating the local inflammatory environment at the defect site, but also release cytokines that promote stem cell migration, osteogenesis, and angiogenesis differentiation, including stromal cell-derived factor-1, bone morphogenetic protein-2, and vascular endothelial growth factor.[7] However, bone defect sites are often accompanied by an imbalance in inflammatory regulation, manifested as a long-term pro-inflammatory response, which hinders the transition of macrophages from M1 to M2, thereby delaying bone regeneration.[8] Therefore, regulating the immune microenvironment around the bone defect, optimizing the transition from M1 to M2, and timely terminating the pro-inflammatory response can better achieve bone regeneration. To solve this problem, various functional bone tissue engineering scaffolds have been developed.[9–11] However, scaffolds with natural acellular extracellular matrix materials as the core have been extensively studied for their multiple advantages, such as low immunogenicity, high biocompatibility, and biodegradability.[12,13]

As a major fishing country, China produces a large amount of fish waste every year, of which fish scales account for about 15%, which is a low-cost and easily accessible biological resource.[14] Fish scales are mainly composed of hydroxyapatite and type I collagen fibers and have a highly ordered three-dimensional structure.[15] Their structure and composition are very similar to bone tissue. Collagen fibers arranged in a special "Bouligand"

[a]*Department of Orthopedics, Peking University Third Hospital, No. 49 North Garden Road, Haidian, Beijing, 100191, China*

[b]*Engineering Research Center of Bone and Joint Precision Medicine, Peking University Third Hospital, No. 49 North Garden Road, Haidian, Beijing, 100191, China. E-mail: sushilong2020@163.com; wangruideng0467@bjmu.edu.cn; med_bai.jinwu@stu.pku.edu.cn; gaoshan@bjmu.edu.cn; zhouf@bjmu.edu.cn; Tel: +86-01082266699*

[c]*Department of Orthopedics, Beijing Friendship Hospital, Capital Medical University, No. 95 Yong'an Road, Xicheng, Beijing, 100050, China. E-mail: rubingzhou@pku.edu.cn*

† Electronic supplementary information (ESI) available. See DOI: https://doi.org/10.1039/d5ra01932j

structure and needle-shaped hydroxyapatite crystals distributed in the collagen fibers give fish scales excellent mechanical strength, good biocompatibility, and the ability to induce osteogenic differentiation.[16–18] Several recent studies have used fish scales as scaffold materials for bone defect repair.[14,17,19] In addition, there are radial grooves and annular ridges on the surface of fish scales. This topological structure may affect important cell behaviors such as cell adhesion, proliferation, and migration.[20] Therefore, acellular fish scale scaffolds (AFS) are promising scaffolds for bone tissue engineering.

In recent years, the strategy of using mussel-inspired polydopamine (PDA) to functionalize the surface of scaffold materials has received widespread attention. Due to the complex surface shape of some scaffolds and a limited line of sight, many surface modification methods are not suitable.[21] By simply dipping the scaffold in an aqueous dopamine solution, PDA can easily form a 50 nanometer-thick coating on the surface of the scaffold.[22] This method is particularly suitable for scaffolds with complex surface shapes. The formation mechanism of PDA coating is mainly based on the oxidative autopolymerization of dopamine molecules under alkaline conditions and the strong adhesion of catechol and amino groups of dopamine.[23] PDA coatings have efficient redox capabilities to remove potential ROS due to their large number of reducing groups, such as phenol and catechol.[24,25] PDA also has immunomodulatory activity, reducing M1 macrophage polarization to down-regulate inflammatory cytokines, and activating M2 macrophage polarization.[26,27] In addition, PDA coating can also enhance the adhesion, proliferation, and osteogenic differentiation of BMSCs, as well as accelerate new bone formation and enhance osseointegration.[28,29] This evidence suggests the huge potential of PDA in bone regeneration.

Therefore, from the above viewpoint, integration of AFS with PDA would provide a new strategy for the treatment of bone defects. In our study, PDA was used to functionalize AFS to obtain PDA-functionalized acellular fish scale scaffolds (PDA-AFS). We used a novel decellularization scheme to prepare AFS, then dipped AFS in dopamine solution and freeze-dried to obtain PDA-AFS. We hypothesized that PDA-AFS has ROS scavenging activity, osteo-immunomodulation, and osteogenic abilities for bone defect repair. In this study, we evaluated the application potential of scaffolds for bone regeneration through multiple aspects such as scaffold characterization, cytocompatibility, ROS scavenging activity, immunomodulation, and osteogenic differentiation ability *in vitro* and *in vivo*, and their potential mechanisms (Fig. 1).

2. Materials and methods

2.1. Materials

Fish scales were isolated from Grass carps obtained from a commercial dealer in Beijing, China. Tris–hydrochloride

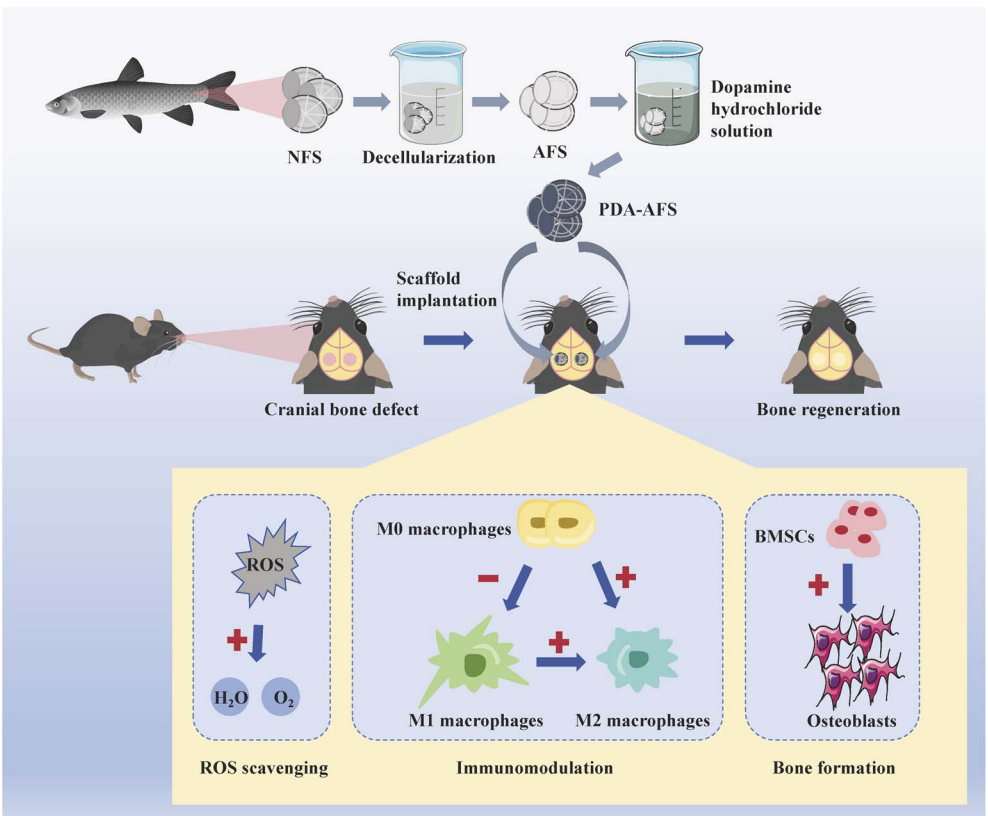

Fig. 1 Schematic illustration of a polydopamine-functionalized acellular fish scale scaffold (PDA-AFS) with reactive oxygen species (ROS) scavenging, immunomodulation, and osteogenic differentiation ability for cranial bone defect repair. NFS: native fish scales; AFS: acellular fish scale scaffolds; BMSCs: bone marrow mesenchymal stem cells.

(Tris–HCl), Triton X-100, ethylenediamine tetraacetic acid (EDTA), and ribonuclease A were procured from Bioroyee Co., Ltd (Beijing, China). Deoxyribonuclease I was procured from Mreda Co., Ltd (Beijing, China). Fetal bovine serum (FBS), α-MEM, DMEM, penicillin–streptomycin, and trypsin were purchased from Gibco Life Technologies Co., Ltd (Grand Island, USA). Dexamethasone, ascorbic acid, β-sodium glycerol 3-phosphate, bovine serum albumin (BSA), and phosphate buffered saline (PBS) were purchased from Solarbio Science & Technology Co., Ltd (Beijing, China).

2.2. Preparation of scaffolds

First, AFS was prepared using a novel decellularization scheme.[30] The native fish scales (NFS), measuring 2–3 cm in diameter, had their epidermis, fascia, and other soft tissues removed with forceps and scalpels, and were rinsed five times with distilled water. Next, fish scales were treated with 10 mM Tris–HCl buffer containing 0.1% EDTA at 4 °C for 24 hours, and the cellular components of fish scales were removed with 1% Triton X-100 at 4 °C for 4 days. Then, fish scales were digested with nuclease solution (containing 500 U per mL deoxyribonuclease I and 1 mg per mL ribonuclease A) at 37 °C for 24 hours and washed with distilled water 5 times. After that, AFS was immersed in dopamine hydrochloride solution (2 mg mL^{-1} in 10 mM Tris–HCl buffer, pH 8.5) at room temperature for 24 hours under mechanical stirring to promote dopamine's oxidation and polymerization. All the scaffolds were carefully washed with distilled water 5 times. Finally, AFS and PDA-AFS were sterilized with 75% ethanol and ultraviolet, freeze-dried, and stored for later use.

2.3. Characterization of scaffolds

2.3.1. Decellularization effect evaluation. We used histological staining and DNA residence analysis to evaluate the decellularization effect at both qualitative and quantitative levels. NFS and AFS were sectioned into 5 μm slices and stained with hematoxylin and eosin (H&E), 4′,6-diamidino-2-phenylindole (DAPI), and picrosirius red (PR). The marine animal tissue genomic DNA extraction kit (Bioroyee, China) was used to quantify the total DNA content of NFS and AFS ($n = 5$).

2.3.2. FTIR analysis. NFS, AFS, and PDA-AFS were embedded in paraffin and sectioned into 5 μm slices. After overnight drying under vacuum followed by dewaxing, the sections were evaluated with Fourier transform infrared spectroscopy (FTIR) (Thermo Fisher Scientific, USA) to obtain infrared spectra ($n = 5$).[31,32] The amide I (1720–1590 cm^{-1}) and phosphate (1200–900 cm^{-1}) peaks were respectively used to semi-quantitatively characterize the contents of collagen and hydroxyapatite of scaffolds.[32,33]

2.3.3. Scanning electron microscopy (SEM). SEM and energy-dispersive X-ray spectroscopy (EDS) (JSM-7900F, JEOL, Japan) were used to observe and capture images of the surface morphology and element distribution of scaffolds. Prior to imaging, all samples were coated with a thin gold layer.

2.3.4. Swelling test. The initial weight of the freeze-dried scaffolds (M_0) was noted. Subsequently, the scaffolds were submerged in phosphate buffered saline (PBS) with a pH of 7.4 at 37 °C for 48 hours ($n = 5$). The wet weight of each scaffold (M_1) was then determined. The swelling rate was calculated as follows:

$$\text{Swelling rate} = (M_1 - M_0)/M_0 \times 100\%$$

2.3.5. *In vitro* degradation. The scaffolds were fully swollen in PBS (pH = 7.4) at 37 °C for 48 hours, and the weight (W_0) was recorded ($n = 5$). Subsequently, the remaining weight (W_t) of the scaffolds was recorded at different weeks (2, 4, 6, and 8 weeks). The degradation rate was calculated as follows:

$$\text{Degradation rate} = (W_0 - W_t)/W_0 \times 100\%$$

2.3.6. Mechanical test. Before testing, the scaffolds were trimmed to 5 mm × 5 mm in size and then tested with atomic force microscope (AFM) (Bruker, Germany) to collect force–displacement curves ($n = 3$). The force–displacement curve was fitted by the Hertzian model using Nanoscope Analysis software (Version 3.0, Bruker, Germany) to determine Young's modulus of the scaffolds.

2.4. *In vitro* experiments

2.4.1. Cell viability and proliferation. BMSCs (2×10^4 cells, passage 4) were seeded onto the scaffolds ($n = 3$). After 1 and 3 days of culture, a live/dead cell kit (Servicebio, China) was used to detect the cell viability according to the instructions. In addition, the cell counting kit-8 (CCK-8) (Fude Biological, China) was used to evaluate cell proliferation on days 1, 3, 5, and 7.

2.4.2. Cell adhesion and morphology. Fluorescence microscopy and SEM visualized cell adhesion and morphology. Specifically, BMSCs (2×10^4 cells, passage 4) were seeded onto AFS and PDA-AFS ($n = 3$) and cultured for 1 and 3 days. Scaffolds with cells were fixed with 4% paraformaldehyde. The cytoskeleton and nucleus were stained with FITC-phalloidin and DAPI (Solarbio, China), respectively, and then observed with a fluorescence microscope (Nikon, Japan). For SEM observation, scaffolds with cells were fixed in 2.5% glutaraldehyde, dehydrated with gradient ethanol, and critical-point dried. Finally, scaffolds with cells were sputter-coated with gold and observed using SEM (JSM-7900F, JEOL, Japan).

2.4.3. ROS scavenging activity

2.4.3.1 1,1-Diphenyl-2-picrylhydrazyl (DPPH) scavenging efficiency. The ROS scavenging activity of scaffolds was evaluated *in vitro* using the DPPH assay. The DPPH scavenging efficiency was determined using the DPPH scavenging efficiency assay kit (Yuanye, China) according to the instructions. Vitamin C (40 μg mL^{-1}) was used as the positive control group, and the scaffold was not placed as the negative control group ($n = 5$).

2.4.3.2 Cell protective effect. The protective effect of scaffolds on cells against oxidative stress induced by H_2O_2 treatment was evaluated using a live/dead cell kit (Servicebio, China) and CCK-8 (Fude Biological, China). BMSCs (2×10^4 cells, passage 4)

were seeded in 48-well plates and cultured for 24 hours, then scaffolds were added and the medium was replaced with medium containing 200 μM H_2O_2 ($n = 5$). Cells grown without H_2O_2 and scaffolds served as the control group. After another 24 hours of culture, scaffolds, and medium were removed, and cell viability was assessed using a live/dead cell kit and CCK8, respectively.

2.4.3.3 Intracellular ROS detection. BMSCs (2×10^4 cells, passage 4) were seeded in 48-well plates and cultured for 24 hours, then scaffolds were added and the medium was replaced with medium containing 200 μM H_2O_2 ($n = 5$). Cells without scaffolds and H_2O_2 were used as the control group. After another 2 hours of culture, a reactive oxygen species assay kit (2′,7′-dichloro fluorescein diacetate, DCFH-DA, Beyotime, China) was used to evaluate the effect of scaffolds on intracellular ROS production induced by oxidative stress. Finally, cells were observed using a fluorescent microscope (Nikon, Japan) and quantified using a multifunctional microplate reader with an excitation wavelength of 488 nm and an emission wavelength of 525 nm (Molecular Devices, USA).

2.4.4. Immunomodulation and osteogenic differentiation *in vitro*

2.4.4.1 Enzyme-linked immunosorbent assay (ELISA). A co-culture system of RAW264.7 cells and scaffolds was used to evaluate the immunomodulatory performance of scaffolds. RAW264.7 cells (5×10^3 cells) were seeded on the scaffolds and cultured for 3 days ($n = 5$). A blank group and a lipopolysaccharide (LPS) group (200 ng mL^{-1}) were set up simultaneously. The cell supernatant was collected and tumor necrosis factor-α (TNF-α) and IL-10 contents were measured according to the instructions of the ELISA kits (Multisciences, China).

2.4.4.2 Alkaline phosphatase (ALP) staining and ALP activity. BMSCs (1×10^4 cells, passage 3) were co-cultured with the scaffolds and the osteogenic induction medium was added ($n = 3$). After 7 and 14 days of culture, cells were fixed with 4% paraformaldehyde and then stained using an ALP staining kit (Beyotime, China). In addition, the ALP value was determined using an ALP assay kit (Beyotime, China), and the ALP activity of each well was normalized to the total protein content of the corresponding supernatant determined by a BCA protein assay kit (Beyotime, China).

2.4.4.3 Alizarin red staining (ARS). After 21 days of osteogenic induction, cells were fixed with 4% paraformaldehyde and stained using an ARS kit (Solarbio, China) ($n = 3$). After observing the results, the stained calcium nodules were dissolved by immersing them in 10% cetylpyridinium chloride solution, and then the absorbance was measured at 570 nm using a Microplate Reader (Molecular Devices, USA).

2.4.4.4 Immunofluorescent (IF) staining. After 3 days of co-culture of RAW264.7 cells with scaffolds and 14 days of osteogenic induction of BMSCs with scaffolds ($n = 3$), cells were fixed, permeabilized, and blocked. Then, specific primary antibodies were incubated overnight at 4 °C. The relevant primary antibodies are as follows: CD86 (13395-1-AP, Proteintech, 1 : 200), CD206 (18704-1-AP, Proteintech, 1 : 200), RUNX2 (20700-1-AP, Proteintech, 1 : 100), OPN (22952-1-AP, Proteintech, 1 : 200) and COL-1α (14695-1-AP, Proteintech, 1 : 100). The next day, cells were labeled with fluorescent secondary antibodies, cell nuclei were stained with DAPI (Solarbio, China), and observed under a fluorescence microscope (Nikon, Japan).

2.4.4.5 Quantitative real-time PCR (qRT-PCR). The expression of CD86, CD206, RUNX2, OPN, and COL-1α was detected by qRT-PCR. Briefly, RAW264.7 cells were co-cultured with scaffolds for 3 days and BMSCs were induced with scaffolds for 14 days ($n = 3$), total RNA from RAW264.7 cells or BMSCs was extracted using an RNA extraction kit (Accurate Biotechnology, China), and cDNA was obtained using a reverse transcription kit (Accurate Biotechnology, China). The qRT-PCR was performed using a real-time PCR system. mRNA levels were assessed and further normalized to endogenous control GAPDH. The primers used are listed in Table S1.†

2.4.4.6 RNA sequencing. After 14 days of osteogenic induction of BMSCs with PDA-AFS, transcriptome analysis was performed. Briefly, cells were collected and total RNA was extracted using Trizol reagent ($n = 3$). Samples were sent to Majorbio Biotechnology Co., Ltd (Shanghai, China) to perform RNA purification, reverse transcription, library construction and sequencing. Differential expression analysis, Gene Ontology (GO) terms enrichment analysis, and Kyoto Encyclopedia of Genes and Genomes (KEGG) pathway enrichment analysis were performed using the Majorbio Cloud Platform (**https://www.majorbio.com**).

2.5. *In vivo* experiments

2.5.1. Cranial bone defect model. Animal experiments were approved by the Animal Care and Use Committee of Peking University Health Science Center (DLASBD0205). 8 week-old male C57BL/6J mice were anesthetized with 2.5% pentobarbital, and 2 circular full-thickness bone defects with a diameter of 3 mm were made on both sides of the top of the skull. AFS and PDA-AFS were implanted in the bone defects, respectively, and no scaffold was placed in the control group. The periosteum was protected and retained during the operation. Mice were euthanized 4 and 8 weeks after surgery, and skulls, hearts, livers, spleens, lungs, and kidneys were obtained and fixed with 4% paraformaldehyde.

2.5.2. Micro-CT analysis. The skulls of all mice were scanned with micro-CT (Siemens, Germany). After the scan data were obtained, the skulls were three-dimensional visualized and reconstructed by software, and the percentage of bone volume relative to tissue volume (BV/TV) and bone mineral density (BMD) of each sample were calculated.

2.5.3. Histological evaluation. After micro-CT scanning, the skulls were decalcified, dehydrated, and embedded in paraffin. The specimens were cut into 5 μm sections across the center of the bone defect, followed by H&E and Masson trichrome staining. In addition, immunohistochemical (IHC) staining of RUNX2 and OCN was performed to further analyze osteogenesis. Hearts, livers, spleens, lungs, and kidneys were sliced and stained with HE to evaluate the biosafety of scaffolds *in vivo*.

2.6. Statistical analysis

The analyses were performed using GraphPad Prism 10 software. The quantitative data were presented as mean ± standard

deviation. The Student's *t*-test was performed for two-group comparisons. One-way or two-way analysis of variance with Tukey's post hoc test was analyzed for more than two groups. Statistical significance was defined as $p < 0.05$ (ns: no significant differences, *: $p < 0.05$, **: $p < 0.01$, ***: $p < 0.001$, ****: $p < 0.0001$).

3. Results

3.1. Characterization of scaffolds

The NFS were harvested from grass carp and decellularized. After decellularization, compared with NFS, the fish skin on the surface of AFS was completely removed. AFS became more transparent, and the ridges and grooves on its surface were well preserved (Fig. 2A). H&E and DAPI staining of AFS did not show extensive nuclei. PR staining showed that AFS was rich in collagen and the content was not significantly reduced. Quantitatively, the DNA content in AFS was significantly less and less than 50 ng mg^{-1} (Fig. 2A), which was the minimum criterion for successful decellularization.[34] Fish scales are mainly composed of collagen and hydroxyapatite. We innovatively used FTIR to quantitatively evaluate the reduction in collagen and hydroxyapatite contents in AFS (Fig. 2B). The results showed that the collagen and hydroxyapatite contents of AFS decreased by about 28.56% and 28.93% compared with NFS, respectively. In addition, we also found that due to the functionalization of PDA, the amide I peak of PDA-AFS shifted backward, which was caused by the vibrations of C=C of the aromatic cycles of PDA at 1598 cm^{-1}.[35]

After PDA functionalization, PDA-AFS appeared tan. The microstructure of the scaffold surface was observed by SEM (Fig. 2C). The AFS surface had a directional three-dimensional topological microstructure, characterized by regularly arranged ridges and grooves. PDA-AFS had a similar surface microstructure, but because of the coverage of PDA, the ridges and grooves were smoother. EDS elemental mapping was used to analyze the distribution of C, N, O, Ca, and P elements on the scaffold surface. The distribution of the above elements on the surfaces of AFS and PDA-AFS was homogeneous and similar. The swelling rates of the two kinds of scaffolds were similar (Fig. 2D). During *in vitro* degradation, neither scaffold completely degraded at 8 weeks. There was no statistical difference in their degradation rates at 2, 4, and 6 weeks, but at 8 weeks, the degradation rate of AFS was significantly higher. The 8 week degradation rates for AFS and PDA-AFS were 36.18 $\pm$ 1.71% and 32.13 $\pm$ 1.85%, respectively (Fig. 2E). In addition, the Young's modulus of AFS and PDA-AFS were 5.84 $\pm$ 1.21 GPa and 5.81 $\pm$ 1.90 GPa, respectively. There was no significant difference in Young's modulus between them (Fig. 2F).

3.2. Cytocompatibility of scaffolds

The cytocompatibility of the scaffolds was evaluated by detecting the viability, proliferation, and adhesion of BMSCs on the scaffold surface. After 1 and 3 days of culture, live/dead staining showed that most of the BMSCs were stained with fluorescent green (living cells), and very few were red (dead cells) (Fig. 3A). Quantitative analysis showed that the cell viability of the two kinds of scaffolds were similar and both were above 95%, and there was no difference with the control group (Fig. 3B). We also found that the cells on the scaffold surface grew along the topological structure of the scaffold surface and showed a regular arrangement, and the cells on the PDA-AFS surface were more obvious. We used CCK-8 to evaluate the proliferation of BMSCs on the scaffolds on days 1, 3, 5, and 7. As shown in Fig. 3C, the number of BMSCs increased with the extension of culture time. There was no significant difference in the proliferation level at each time point compared with the control group.

We used fluorescence microscopy and SEM to observe the adhesion morphology of BMSCs on the scaffold. After 1 and 3 days of culture, DAPI and phalloidin were used for staining (Fig. 3D). BMSCs were long spindle-shaped and grew along the ridges and grooves on the scaffold surface, among which the cells on PDA-AFS adhered more tightly. As cells proliferated and their number increased, the arrangement of cells on AFS became increasingly chaotic, while the cells on PDA-AFS still showed regular arrangement, showing better adhesion. Similar results were observed by SEM (Fig. 3E). BMSCs on PDA-AFS extended more pseudopodia, were flatter, and adhered more tightly.

3.3. ROS scavenging activity of scaffolds

We evaluated the ROS scavenging activity of scaffolds based on *in vitro* DPPH scavenging efficiency, cytoprotective effect, and intracellular ROS scavenging ability. We first conducted a DPPH assay and found that the DPPH scavenging efficiency of PDA-AFS (84.87 $\pm$ 3.12%) was higher than that of AFS (13.71 $\pm$ 2.57%) and was comparable to that of the antioxidant vitamin C (87.39 $\pm$ 0.35%) (Fig. 4A). This demonstrated the excellent antioxidant ability of PDA-AFS. We further explored the protective effect of scaffolds on BMSCs under H_2O_2-induced oxidative stress. After co-culture with H_2O_2 for 24 hours, cell viability was evaluated using live/dead staining and CCK-8. The results showed that a large number of dead cells appeared in the control group after co-culture with H_2O_2. When scaffolds were added, this situation was significantly improved and dead cells were significantly reduced (Fig. 4B). CCK-8 also showed similar results. Notably, compared to AFS, PDA-AFS treated cells showed higher cell viability after exposure to H_2O_2, only slightly lower than the control group (Fig. 4C). To further demonstrate the ROS scavenging properties of PDA-AFS, the intracellular ROS levels of BMSCs after co-culture with two kinds of scaffolds were studied using the DCFH-DA probe (Fig. 4D). The PDA-AFS group showed the lowest fluorescence intensity. Quantitative fluorescence intensity showed that the fluorescence intensity of the PDA-AFS group was comparable to that of the control group (Fig. 4E). These results demonstrated that PDA-AFS had good ROS scavenging activity.

3.4. Immunomodulation of scaffolds

Immunomodulation plays an important role in the process of bone regeneration. In our study, we co-cultured RAW264.7 cells

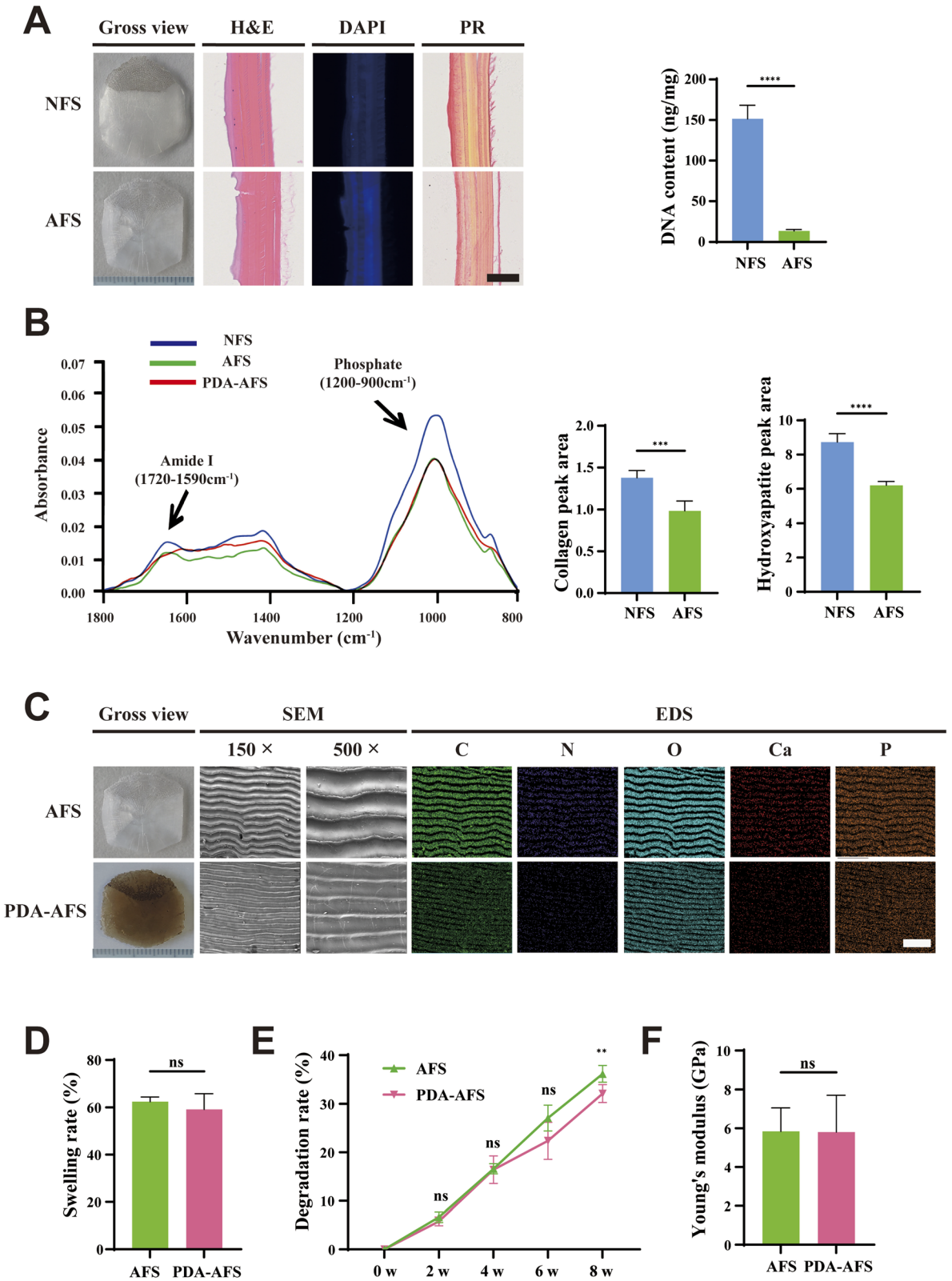

Fig. 2 Characterization of scaffolds. (A) Macroscopic features, histological staining, and DNA content of NFS and AFS. Scale bar = 100 μm. (B) Characteristic FTIR spectrum for NFS, AFS, and PDA-AFS. Collagen and hydroxyapatite contents of NFS and AFS. (C) Macroscopic features, SEM, and EDS elemental mapping images of AFS and PDA-AFS. Scale bar = 250 μm. The swelling rates (D), degradation rates at 2 weeks, 4 weeks, 6 weeks, and 8 weeks (E), and Young's modulus (F) of AFS and PDA-AFS. All values are presented as means ± standard deviation (ns: no significant differences, *: $p < 0.05$, **: $p < 0.01$, ***: $p < 0.001$, ****: $p < 0.0001$).

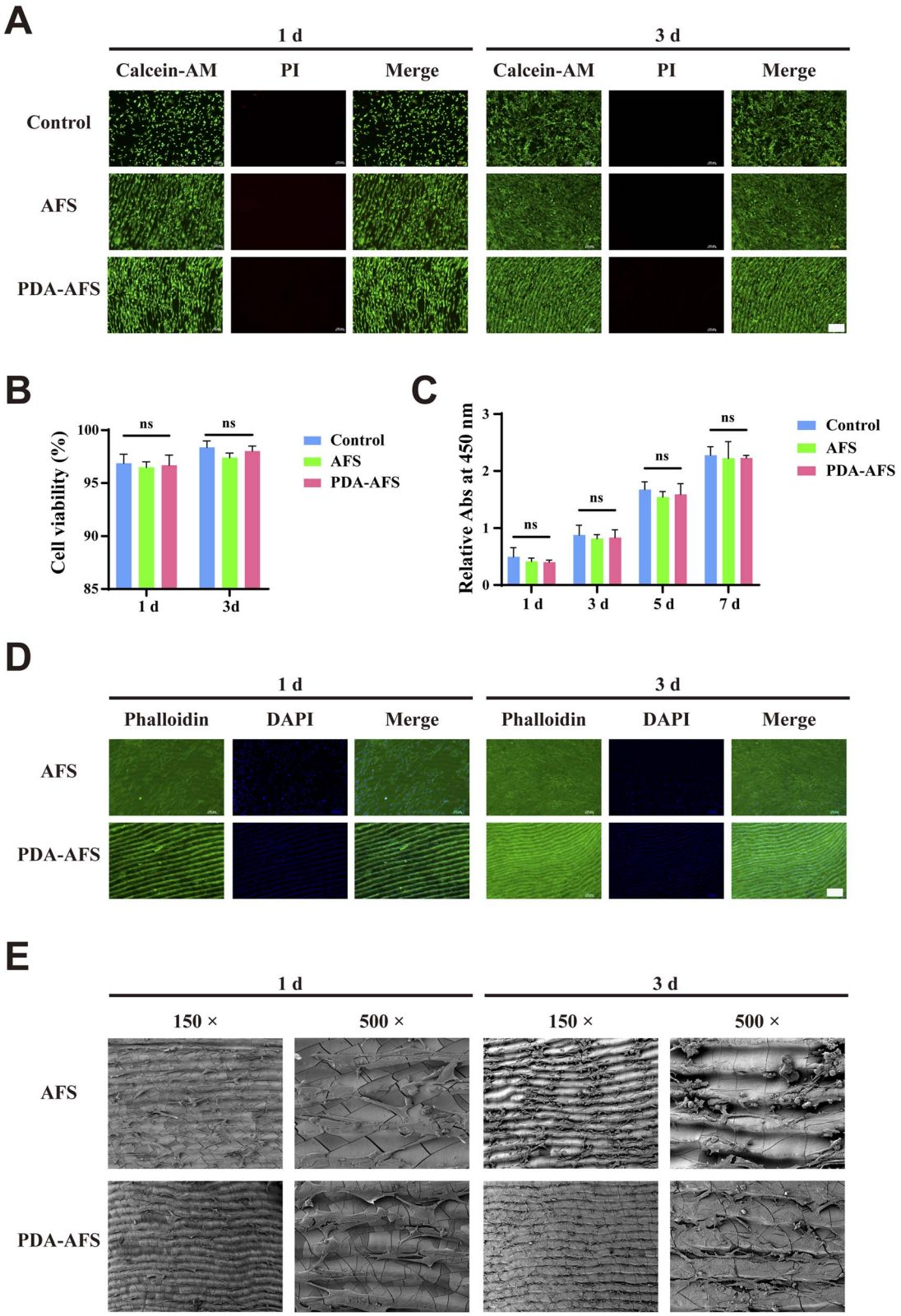

Fig. 3 Cytocompatibility of scaffolds. (A) Live/dead staining of scaffolds on which BMSCs had been seeded at 1 and 3 days. The representative images show the live (green) and dead (red) cells. Scale bar = 200 μm. (B) Cell viability of scaffolds on which BMSCs had been seeded at 1 and 3 days. (C) Cell proliferation of scaffolds evaluated by CCK-8. (D) Fluorescence microscopy images of the phalloidin/DAPI staining of BMSCs cultured on the scaffolds at 1 and 3 days. Scale bar = 200 μm. (E) SEM images of BMSCs cultured on the scaffolds at 1 and 3 days. All values are presented as means ± standard deviation (ns: no significant differences, *: $p < 0.05$, **: $p < 0.01$, ***: $p < 0.001$, ****: $p < 0.0001$).

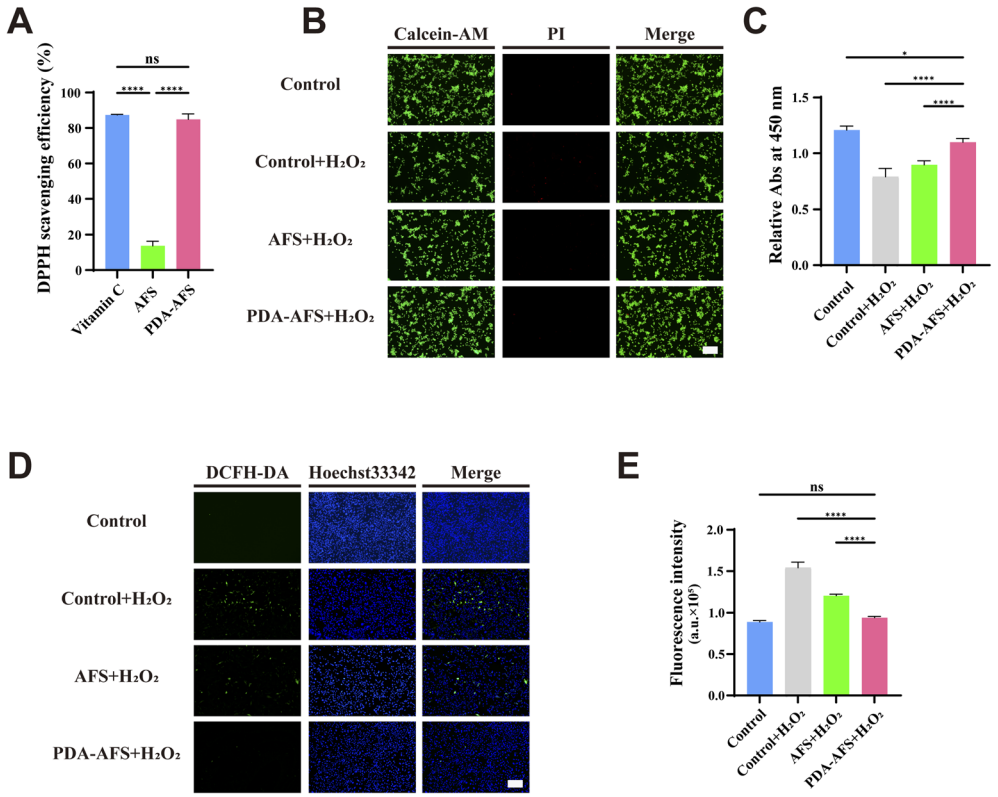

Fig. 4 ROS scavenging activity of scaffolds. (A) DPPH scavenging efficiency of scaffolds. (B) Live/dead staining of BMSCs after co-culture with scaffolds and H_2O_2 for 24 hours. Scale bar = 200 μm. (C) Cell viability of BMSCs evaluated by CCK-8 after co-culture with scaffolds and H_2O_2 for 24 hours. (D) Fluorescence microscopy images of DCFH-DA/Hoechst 33342 staining of BMSCs after co-culture with scaffolds and H_2O_2 for 2 hours. Scale bar = 200 μm. (E) Fluorescence intensity of DCFH-DA of BMSCs. All values are presented as means ± standard deviation (ns: no significant differences, *: $p < 0.05$, **: $p < 0.01$, ***: $p < 0.001$, ****: $p < 0.0001$).

with scaffolds to evaluate the effect of scaffolds on macrophage polarization, and then evaluate the immunomodulatory effect of scaffolds. Cells added with LPS were set as the positive control group. Cell supernatants were first collected to measure the contents of TNF-α and IL-10, and then the expression of the M1 marker (CD86) and M2 marker (CD206) was also assessed. As shown in Fig. 5A, the TNF-α content in the PDA-AFS group was significantly lower than that in the AFS group but was also significantly higher than that in the control group. The TNF-α content in the LPS group was much higher than that in the other three groups. Regarding IL-10 content (Fig. 5B), the PDA-AFS group was significantly higher than other groups. Judging from IF staining and mRNA expression (Fig. 5C and D), the expression levels of CD86 in the PDA-AFS group and the control group were the lowest, but there was no statistical difference in the mRNA expression level of CD86 between the PDA-AFS group and the AFS group. This may be due to the inclusion of data from the LPS group in the analysis, as the mRNA expression level in the LPS group was much higher than in other groups. As for the expression level of CD206, the expression level in the PDA-AFS group was the highest in terms of IF staining and mRNA expression. These results suggested that macrophages stimulated by PDA-AFS tend to polarize to the M2 phenotype rather than the M1 phenotype and secrete more anti-inflammatory cytokines than AFS.

3.5. Osteogenic differentiation *in vitro*

In this study, BMSCs were co-cultured with scaffolds and induced osteogenesis. The ALP activity, calcium deposition, and expression of osteogenic markers were measured at different time points to evaluate their osteogenic induction ability. Early osteogenesis ability was evaluated using ALP staining and ALP assay kit (Fig. 6A). After 7 and 14 days of culture, ALP staining was positive in each group, with the PDA-AFS group showing the highest ALP activity, followed by the AFS group. The quantitative determination results were consistent with the staining results. Calcium nodule deposition is a key marker of advanced osteogenic differentiation, and calcium nodule deposition was assessed by ARS staining (Fig. 6A). After 21 days of culture, calcium nodules appeared in each group, with the most obvious and largest calcium nodules deposition in the PDA-AFS group, followed by the AFS group. Quantitative analysis also showed that the PDA-AFS group had the largest amount of calcium nodule deposition. We also stained for osteogenic markers (RUNX2, OPN, and COL-1α proteins) expressed in BMSCs by IF staining (Fig. 6B and C). After 14 days of culture, the fluorescence intensity of RUNX2, OPN, and COL-1α proteins in the PDA-AFS group was the strongest in all groups. In addition, we also used qRT-PCR to detect the mRNA expression levels of RUNX2, OPN, and COL-1α in different groups of cells after 14

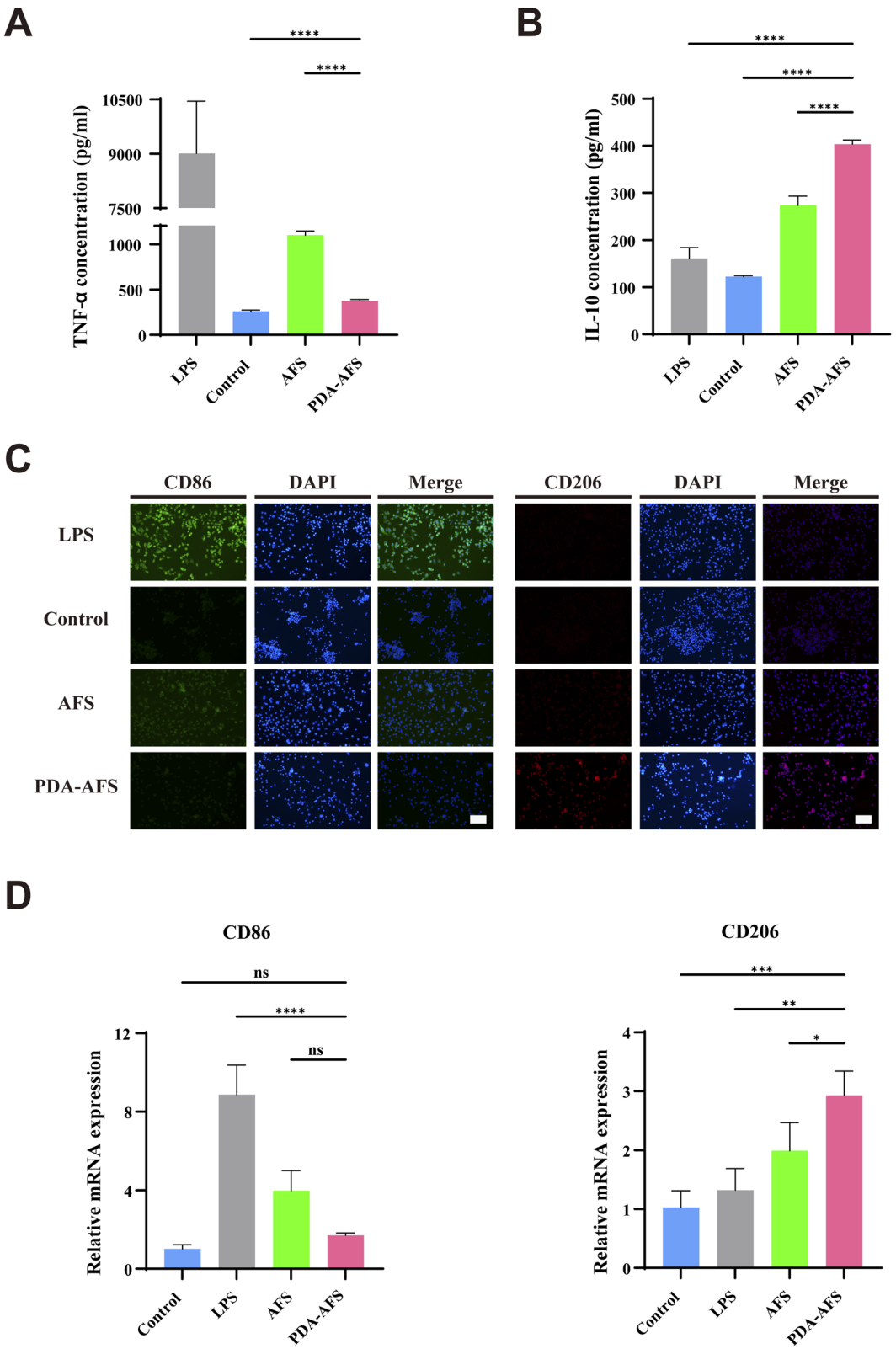

Fig. 5 Immunomodulation of scaffolds. The contents of TNF-α (A) and IL-10 (B) of the supernatants of RAW264.7 cells after co-culture with scaffolds for 3 days. (C) Fluorescence microscopy images of IF staining of CD86 and CD206 in RAW264.7 cells after co-culture with scaffolds for 3 days. Scale bar = 100 μm. (D) The mRNA expression levels of CD86 and CD206 in RAW264.7 cells. All values are presented as means ± standard deviation (ns: no significant differences, *: $p < 0.05$, **: $p < 0.01$, ***: $p < 0.001$, ****: $p < 0.0001$).

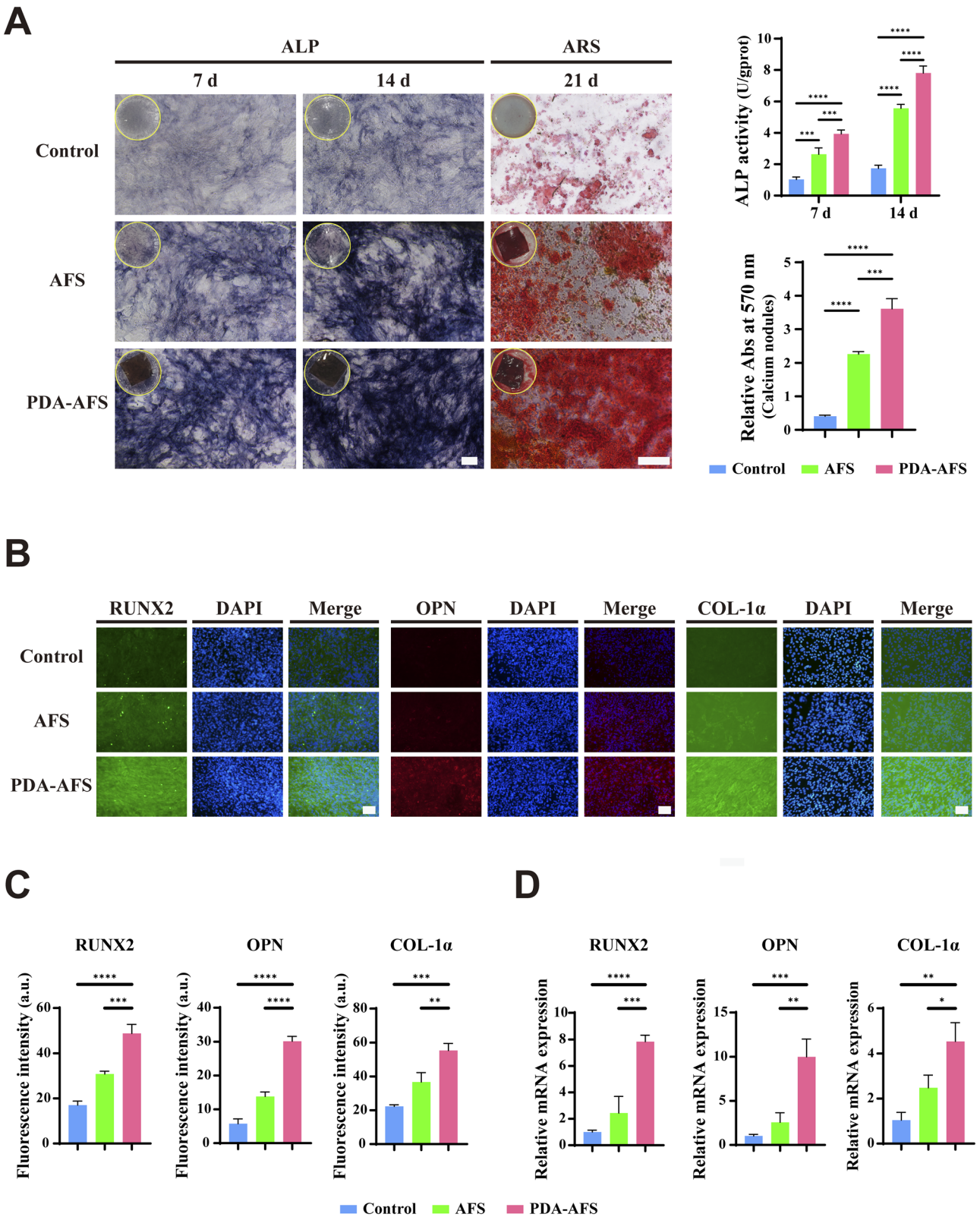

Fig. 6 Osteogenic differentiation ability of scaffolds *in vitro*. (A) ALP staining and ALP activity of BMSCs after 7 and 14 days of osteogenic induction, and ARS staining and quantitative analysis of calcium nodules after 21 days of osteogenic induction. Scale bar = 200 μm. (B and C) Fluorescence microscopy images and quantitative analysis of IF staining of RUNX2, OPN, and COL-1α in BMSCs after 14 days of osteogenic induction. Scale bar = 100 μm. (D) The mRNA expression levels of RUNX2, OPN, and COL-1α in BMSCs after 14 days of osteogenic induction. All values are presented as means ± standard deviation (ns: no significant differences, *: $p < 0.05$, **: $p < 0.01$, ***: $p < 0.001$, ****: $p < 0.0001$).

days of culture (Fig. 6D). Compared with the control and AFS groups, the mRNA expression levels of the above markers were significantly increased in the PDA-AFS group. The above results indicated that PDA-AFS had excellent osteogenic induction ability.

In order to further clarify the potential mechanism of PDA-AFS inducing bone regeneration, cells from the PDA-AFS group and control group were collected for transcriptome analysis after 14 days of culture. Differential expression gene analysis showed that compared with the control group, the PDA-AFS group had 302 gene expressions up-regulated and 174 gene expressions down-regulated, revealing a huge difference in gene expression (Fig. 7A and B). We performed GO and KEGG enrichment analysis for upregulated genes. GO enrichment analysis showed that PDA-AFS may promote osteogenesis by participating in "biomineral tissue development", "bone remodeling", and "bone mineralization" (Fig. 7C). KEGG pathway enrichment analysis showed that these differentially expressed genes were enriched in some pathways, such as "Cytokine–cytokine receptor interaction", "MAPK signaling pathway", "HIF-1 signaling pathway", "PI3K-AKT signaling pathway", "Cell adhesion molecules", and "Calcium signaling

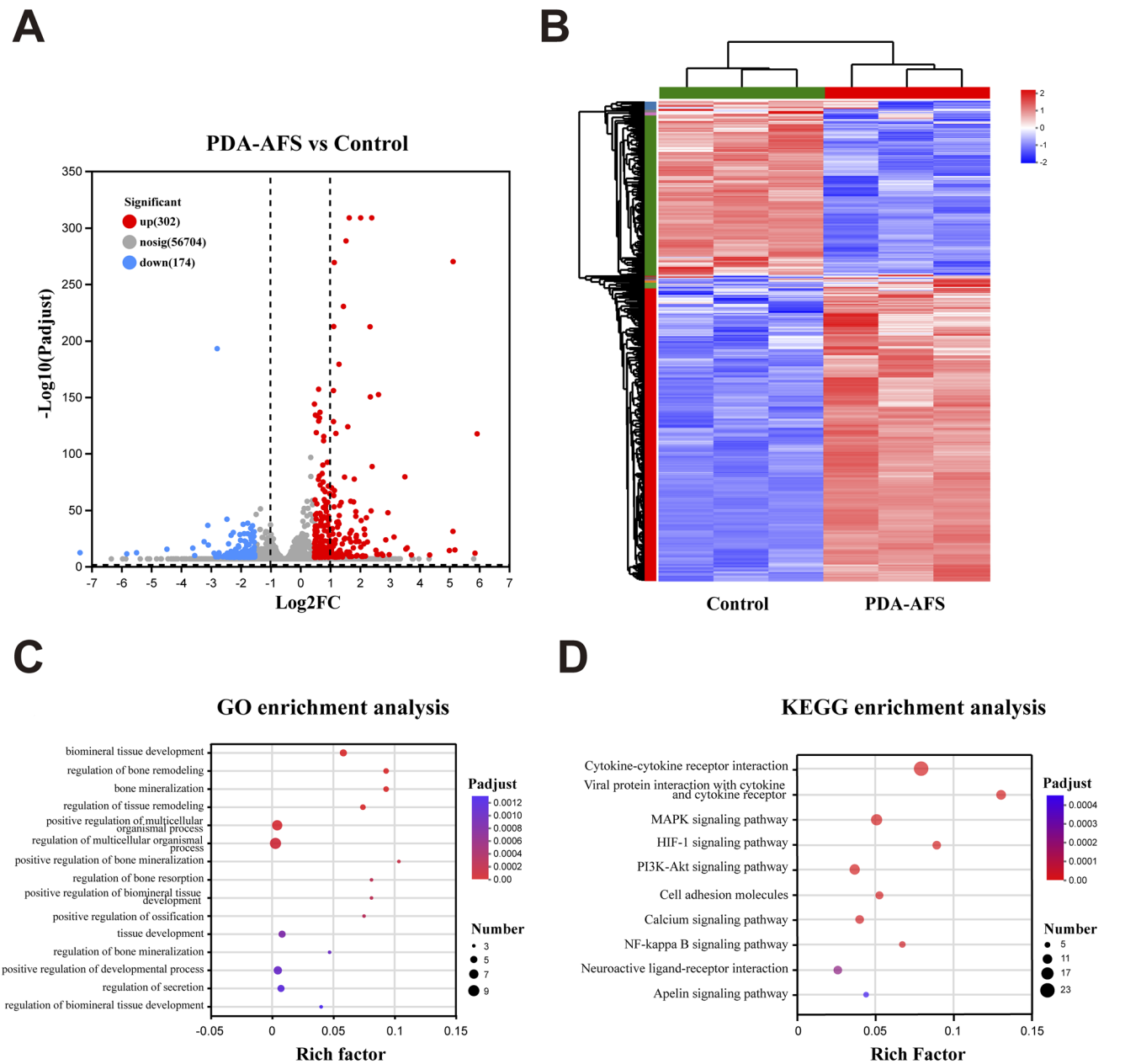

Fig. 7 Transcriptome analysis of BMSCs after 14 days of osteogenic induction. (A) The volcano plot of differentially expressed genes in the PDA-AFS group compared with the control group (P_{adjust} < 0.05, |log 2FC| > 1). (B) Heatmap of differentially expressed genes. (C) Representative up-enrichment of GO terms (category: biological process). (D) The top 10 up-enrichment of KEGG pathways (category: environmental information processing) in the PDA-AFS group compared with the control group. P_{adjust}: the p-value was adjusted for multiple testing.

pathway" (Fig. 7D). The above results suggested that PDA-AFS may promote bone regeneration through the above pathways.

3.6. *In vivo* bone regeneration

In vitro experiments, PDA-AFS showed excellent ROS scavenging activity, immunomodulation, and osteogenic ability. We implanted the scaffolds into mouse cranial bone defect models (3 mm in diameter) to evaluate bone regeneration *in vivo*. Endogenous bone regeneration was assessed by micro-CT and histological staining at 4 and 8 weeks postoperatively. The micro-CT three-dimensional reconstruction in Fig. 8A showed that 4 weeks after surgery, only a very small amount of new bone was formed near the severed ends in the control group. The new bone in the AFS group and PDA-AFS group was more than that in the control group, especially in the PDA-AFS group. Eight weeks after implantation, all groups showed more new bone than before. More importantly, the PDA-AFS group had the most bone formation. From the analysis results of BV/TV and BMD,

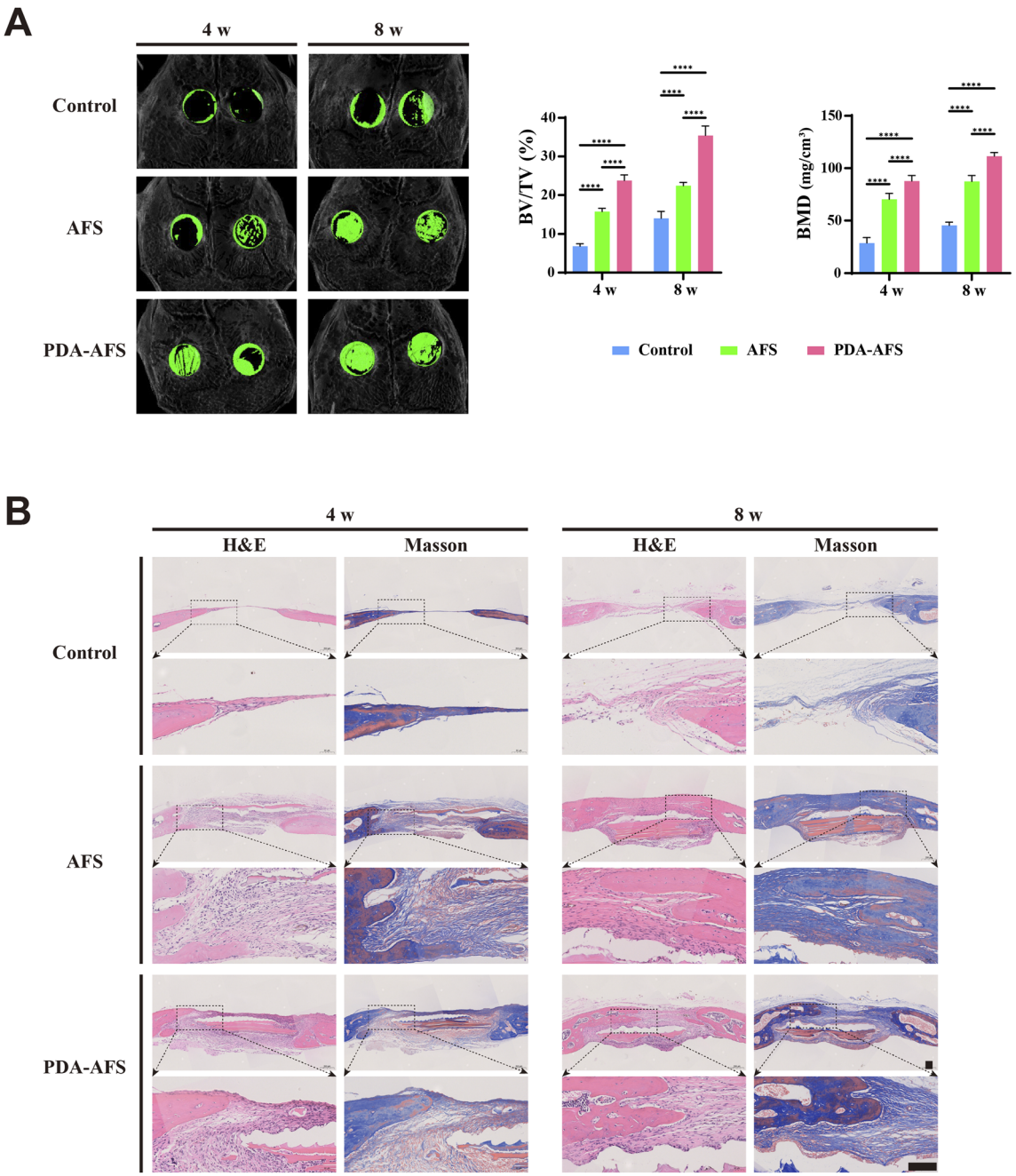

Fig. 8 Bone regeneration ability of scaffolds *in vivo*. (A) Representative three-dimensional reconstructed micro-CT images of mouse skull and quantitative analysis results of BV/TV and BMD at 4 and 8 weeks after surgery. (B) H&E and Masson trichrome staining of bone defect region at 4 and 8 weeks after surgery. Scale bar = 100 μm. All values are presented as means ± standard deviation (ns: no significant differences, *: $p < 0.05$, **: $p < 0.01$, ***: $p < 0.001$, ****: $p < 0.0001$).

the PDA-AFS group also showed the best bone regeneration effect. At 4 and 8 weeks after surgery, the new bone mass in the PDA-AFS group was significantly higher than that in the control group and the AFS group.

H&E and Masson trichrome staining were performed after micro-CT examination (Fig. 8B), further confirming the results of micro-CT. Four weeks after surgery, no obvious new bone was found in the control group, a small amount of new bone appeared in the defect area in the AFS group, and the fibrous tissue and new bone in the PDA-AFS group were more obvious and larger than those in the AFS group. Eight weeks after surgery, a small amount of new bone was also observed in the defect area in the control group, while a large amount of continuous new bone filled the defect in the AFS group and PDA-AFS group. The PDA-AFS group had the highest level of bone regeneration. In addition, we also performed IHC staining to assess the expression levels of osteogenic markers RUNX2 and OCN in the defect area (Fig. 9A). Four weeks after surgery,

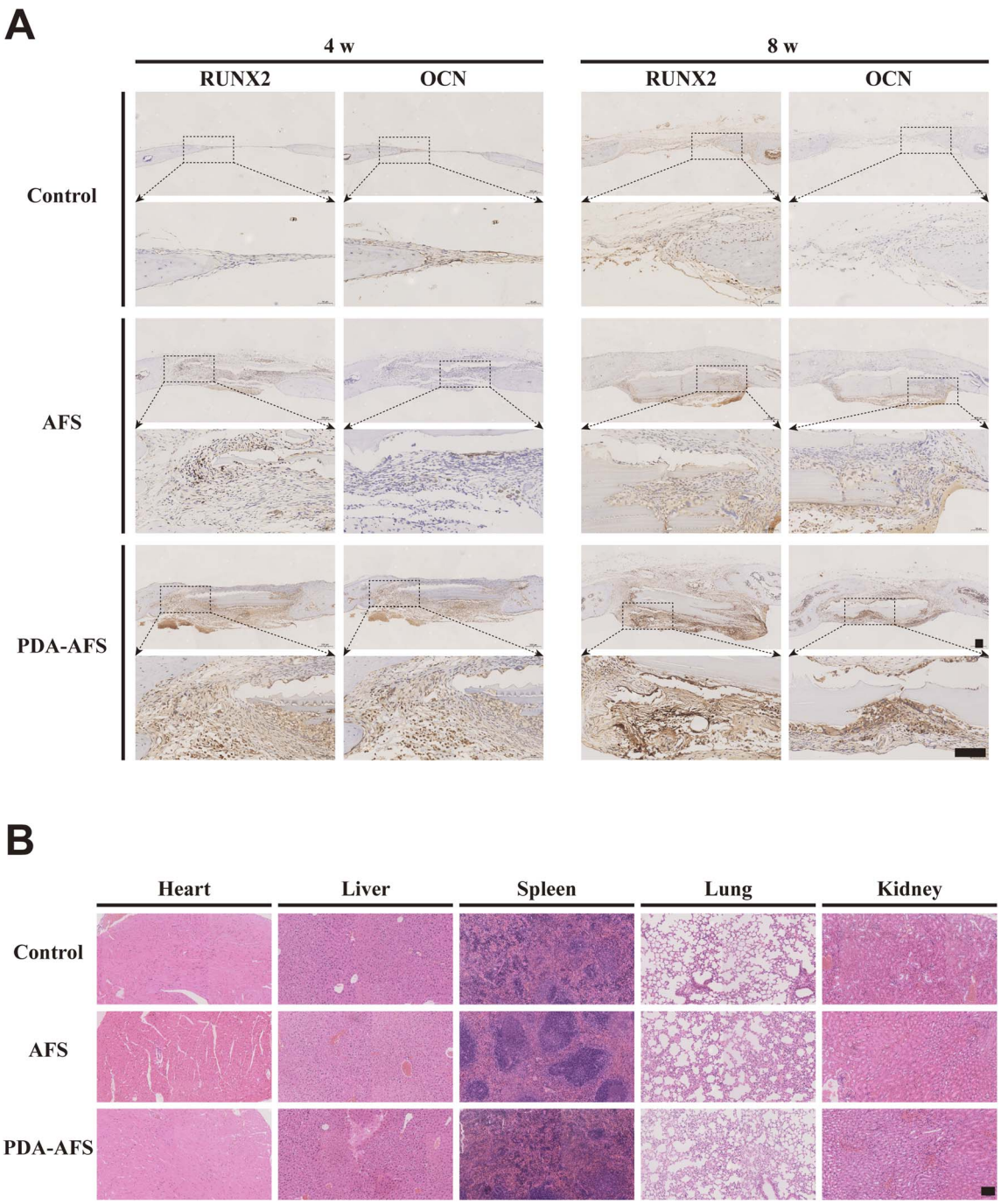

Fig. 9 (A) Immunohistochemical staining of RUNX2 and OCN of bone defect region at 4 and 8 weeks after surgery. Scale bar = 100 μm. (B) H&E-stained samples were obtained from the hearts, livers, spleens, lungs, and kidneys of mice at postoperative week 8. Scale bar = 100 μm.

the expression of RUNX2 and OCN was not significant in the control group, and the expression of OCN was not significant in the AFS group, while both RUNX2 and OCN were significantly expressed in the PDA-AFS group and the expression level was the highest. Eight weeks after surgery, RUNX2 and OCN were significantly expressed in both the AFS group and PDA-AFS group, and the PDA-AFS group also showed the highest expression level. Furthermore, H&E staining images of animal viscera showed that the scaffolds were non-toxic to organisms (Fig. 9B). These results indicated that PDA-AFS had excellent bone regeneration capabilities *in vivo*.

4. Discussion

There are still many problems in the treatment of bone defects, which is a challenge in clinical treatment. In recent years, the continuous development of bone tissue engineering has provided a promising strategy for bone defect repair.[36] There are various scaffold materials designed in the field of bone tissue engineering, including acellular extracellular matrices, metallic materials, organic materials, *etc.*[9,10] They all have their unique advantages and corresponding shortcomings. For example, metal materials have excellent mechanical properties and can provide early mechanical support for bone defects, but they are difficult to degrade, and the degraded heavy metal ions may be toxic.[37] Most acellular extracellular matrix materials have the advantages of low immunogenicity, high biocompatibility, and biodegradability, and have attracted widespread attention, but most acellular extracellular matrix materials have poor mechanical properties.[12,13] Here, we successfully prepared a polydopamine-functionalized acellular fish scale scaffold. It takes natural acellular matrix materials as its core and has the advantages of acellular matrix materials as well as excellent mechanical properties. More importantly, this scaffold not only has good osteogenic ability but also can effectively scavenge ROS, and regulate immunity and inflammation, thereby providing an osteo-friendly microenvironment for bone defect repair. This PDA-AFS scaffold may become a promising bone defect repair material in the field of bone tissue engineering in the future.

Fish scales, as biological wastes, have received little attention. However, recent studies have found that the main components of fish scales are hydroxyapatite and type I collagen fibers, and their calcium-to-phosphorus ratio is similar to that of bone tissue.[15] The AFS obtained after decellularization has good osteogenic differentiation ability and can be used as a scaffold for bone defect repair.[14,17,19] PDA has also received widespread attention due to its special viscosity and can be used for surface functionalization of scaffold materials.[22] Studies have found that PDA coating can not only enhance the osteogenic differentiation of BMSCs but also have efficient redox ability and immunomodulatory activity, which makes it have application prospects in the field of bone regeneration.[24–29] After we functionalized AFS with PDA coating, we gave PDA-AFS more advantages. First, our SEM results showed that the PDA-AFS surface has a regular three-dimensional topological structure, making it an ideal candidate material for three-dimensional tissue engineering. Studies have shown that directional three-dimensional surface topography can trigger specific cellular responses such as adhesion,[38] migration,[39] proliferation, and differentiation,[40] a phenomenon known as contact guidance.[20] Currently, many scaffolds require complex processing methods to fabricate such directional three-dimensional structures, such as aligned electrospinning, directional freezing, and micropatterns, which will lead to controversy about the cost and biocompatibility of these materials.[41] PDA-AFS naturally has this structure and does not require additional processing. Moreover, our results showed that the PDA coating did not destroy the surface structure of the AFS compared to unfunctionalized AFS. The PDA-AFS surface had a similar three-dimensional topography but was smoother. Because of the characteristics of PDA, the surface structure covered by this PDA coating had better cell adhesion than AFS and was more conducive to cell colonization.

As a scaffold for repairing bone defects, excellent mechanical properties are one of its necessary conditions.[42] At present, many scaffolds prepared from decellularized extracellular matrices and hydrogels have good biocompatibility, but their poor mechanical properties are an insurmountable shortcoming.[43,44] However, due to the special "Bouligand" structure of the fish scales, PDA-AFS has extremely excellent mechanical properties. Our results showed that the Young's modulus of PDA-AFS was 5.81 ± 1.90 GPa. The "Bouligand" structure is also called a twisted plywood structure.[45] Its characteristics are briefly introduced: collagen fibrils with a diameter of 100–160 nm embedded with hydroxyapatite nanocrystals form collagen fibers with a diameter of 1 μm, which are in turn assembled into lamellae with a thickness of 50 μm. The orientation of collagen fibers in each lamella is consistent, but adjacent lamellae are misaligned and the direction is 60–75° from each other. Collagen lamellae are arranged layer by layer in this way. The existence of the "Bouligand" structure can improve the mechanical properties of fish scales through multiple mechanisms such as lamellar rotation and separation, collagen fiber tension/compression, fiber delamination, and bridging.[45–48]

High levels of ROS and dysregulated inflammation make the microenvironment in the bone defect site unfavorable for bone regeneration, which is the main reason why bone defects are difficult to treat.[2,3] Studies have confirmed that high levels of ROS are negatively correlated with bone health.[2,49] Early inflammation starts with bone injury, if there is an imbalance, it can manifest itself as a long-term pro-inflammatory response, which can also lead to poor bone regeneration.[8] ROS and inflammation often occur together and form a vicious cycle. Scavenging high levels of ROS and manipulating macrophages to switch from a pro-inflammatory M1 phenotype to a pro-regenerative M2 phenotype to reduce early inflammatory responses can achieve better bone regeneration.[50] This is also a hot topic in the design of various bone tissue engineering scaffolds.[51] PDA coatings contain a large number of reducing groups, such as phenol and catechol, and have an efficient redox ability to remove potential ROS.[24,25] In addition, studies have confirmed that PDA has immunomodulatory activity,

which can reduce the polarization of M1 macrophages, thereby down-regulating inflammatory cytokines, and activating the polarization of M2 macrophages.[26,27] What's even more surprising is that Lin *et al.*'s study reported that AFS also has the effect of promoting the polarization of macrophages towards the M2 phenotype.[41] Our study results confirmed these findings. Compared with AFS and control groups, PDA-AFS had good ROS scavenging activity and can polarize more RAW264.7 cells towards the M2 phenotype and release anti-inflammatory cytokines. Furthermore, compared with the control group, more M2 phenotypic macrophages appeared in the AFS group, which also confirmed the findings of Lin *et al.*[41] PDA-AFS, which had ROS scavenging and immunoregulation capabilities, also achieved better bone regeneration *in vivo* in mouse cranial bone defects. These all indicated the huge application potential of PDA-AFS in the field of bone regeneration. To explore the possible mechanism of PDA-AFS in promoting bone regeneration, we performed transcriptome analysis and the PDA-AFS group showed gene enrichment in "Cytokine–cytokine receptor interaction", "MAPK signaling pathway", "HIF-1 signaling pathway", "PI3K-AKT signaling pathway", "Cell adhesion molecules", and "Calcium signaling pathway". In the future, we can design some molecular biology experiments to further clarify the mechanism of PDA-AFS in promoting bone regeneration.

5. Conclusion

This study proposed a new strategy for designing bone tissue engineering scaffolds based on fish scales and developed a PDA-coated acellular fish scale scaffold, in which PDA was innovatively used to functionalize AFS. PDA-AFS had excellent mechanical properties, special three-dimensional surface topography, and biodegradation. *In vitro*, results showed that PDA-AFS had good biocompatibility and cell adhesion ability, could effectively reduce ROS levels, and had immunomodulatory activity. More importantly, PDA-AFS can enhance osteogenic differentiation of BMSCs and promote endogenous bone regeneration in critical-sized calvarial bone defects. Therefore, based on these characteristics, PDA-AFS is a promising bone tissue engineering scaffold that can be used to promote bone regeneration in bone defects.

Data availability

All relevant data are within the manuscript and its additional files.

Author contributions

Fang Zhou and Shilong Su contributed to the conception and experimental design. Shilong Su, Ruideng Wang, Jinwu Bai, and Rubing Zhou contributed to experimental assays and data collection. Figures were drawn by Shilong Su. Shilong Su and Ruideng Wang analyzed data and draft the manuscript before submission. Fang Zhou and Shan Gao supervised the entire process and revised the manuscript. All authors have read and approved the manuscript.

Conflicts of interest

The authors have no relevant financial or non-financial interests to disclose.

Acknowledgements

This study was supported by the National Natural Science Foundation of China (No. 81971160). The authors would like to thank Shiyanjia Lab (**https://www.shiyanjia.com**) for the AFM analysis.

References

1 J. J. Li, M. Ebied, J. Xu and H. Zreiqat, Current Approaches to Bone Tissue Engineering: The Interface between Biology and Engineering, *Adv. Healthcare Mater.*, 2018, **7**(6), e1701061, DOI: **10.1002/adhm.201701061**.

2 G. Cerqueni, A. Scalzone, C. Licini, P. Gentile and M. Mattioli-Belmonte, Insights into oxidative stress in bone tissue and novel challenges for biomaterials, *Mater. Sci. Eng., C*, 2021, **130**, 112433, DOI: **10.1016/j.msec.2021.112433**.

3 P. Qiu, M. Li, K. Chen, B. Fang, P. Chen, Z. Tang, *et al.*, Periosteal matrix-derived hydrogel promotes bone repair through an early immune regulation coupled with enhanced angio- and osteogenesis, *Biomaterials*, 2020, **227**, 119552, DOI: **10.1016/j.biomaterials.2019.119552**.

4 Q. Chen, P. Shou, C. Zheng, M. Jiang, G. Cao, Q. Yang, *et al.*, Fate decision of mesenchymal stem cells: adipocytes or osteoblasts?, *Cell Death Differ.*, 2016, **23**(7), 1128–1139, DOI: **10.1038/cdd.2015.168**.

5 H. Newman, Y. V. Shih and S. Varghese, Resolution of inflammation in bone regeneration: From understandings to therapeutic applications, *Biomaterials*, 2021, **277**, 121114, DOI: **10.1016/j.biomaterials.2021.121114**.

6 C. Schlundt, T. El Khassawna, A. Serra, A. Dienelt, S. Wendler, H. Schell, *et al.*, Macrophages in bone fracture healing: Their essential role in endochondral ossification, *Bone*, 2018, **106**, 78–89, DOI: **10.1016/j.bone.2015.10.019**.

7 G. Juban and B. Chazaud, Metabolic regulation of macrophages during tissue repair: insights from skeletal muscle regeneration, *FEBS Lett.*, 2017, **591**(19), 3007–3021, DOI: **10.1002/1873-3468.12703**.

8 X. Li, Y. Cheng, P. Gu, C. Zhao, Z. Li, L. Tong, *et al.*, Engineered Microchannel Scaffolds with Instructive Niches Reinforce Endogenous Bone Regeneration by Regulating CSF-1/CSF-1R Pathway, *Adv. Mater.*, 2024, **36**(19), e2310876, DOI: **10.1002/adma.202310876**.

9 Q. Zhang, W. Chen, G. Li, Z. Ma, M. Zhu, Q. Gao, *et al.*, A Factor-Free Hydrogel with ROS Scavenging and Responsive Degradation for Enhanced Diabetic Bone Healing, *Small*, 2024, **20**(24), e2306389, DOI: **10.1002/smll.202306389**.

10 J. Zhao, T. Wang, Y. Zhu, H. Qin, J. Qian, Q. Wang, *et al.*, Enhanced osteogenic and ROS-scavenging MXene

nanosheets incorporated gelatin-based nanocomposite hydrogels for critical-sized calvarial defect repair, *Int. J. Biol. Macromol.*, 2024, **269**(Pt 1), 131914, DOI: 10.1016/j.ijbiomac.2024.131914.

11 X. Xu and J. Song, Segmental long bone regeneration guided by degradable synthetic polymeric scaffolds, *Biomaterials Translational*, 2020, **1**(1), 33–45, DOI: 10.3877/cma.j.issn.2096-112X.2020.01.004.

12 H. Amirazad, M. Dadashpour and N. Zarghami, Application of decellularized bone matrix as a bioscaffold in bone tissue engineering, *J. Biol. Eng.*, 2022, **16**(1), 1, DOI: 10.1186/s13036-021-00282-5.

13 C. W. Cheng, L. D. Solorio and E. Alsberg, Decellularized tissue and cell-derived extracellular matrices as scaffolds for orthopaedic tissue engineering, *Biotechnol. Adv.*, 2014, **32**(2), 462–484, DOI: 10.1016/j.biotechadv.2013.12.012.

14 W. Wu, Z. Zhou, G. Sun, Y. Liu, A. Zhang and X. Chen, Construction and characterization of degradable fish scales for enhancing cellular adhesion and potential using as tissue engineering scaffolds, *Mater. Sci. Eng., C*, 2021, **122**, 111919, DOI: 10.1016/j.msec.2021.111919.

15 H. Feng, X. Li, X. Deng, X. Li, J. Guo, K. Ma, *et al.*, The lamellar structure and biomimetic properties of a fish scale matrix, *RSC Adv.*, 2020, **10**(2), 875–885, DOI: 10.1039/c9ra08189e.

16 H. C. Quan, W. Yang, M. Lapeyriere, E. Schaible, R. O. Ritchie and M. A. Meyers, Structure and Mechanical Adaptability of a Modern Elasmoid Fish Scale from the Common Carp, *Matter*, 2020, **3**(3), 842–863, DOI: 10.1016/j.matt.2020.05.011.

17 Y. Wang, B. Kong, X. Chen, R. Liu, Y. Zhao, Z. Gu, *et al.*, BMSC exosome-enriched acellular fish scale scaffolds promote bone regeneration, *J. Nanobiotechnol.*, 2022, **20**(1), 444, DOI: 10.1186/s12951-022-01646-9.

18 L. Salvatore, N. Gallo, M. L. Natali, L. Campa, P. Lunetti, M. Madaghiele, *et al.*, Marine collagen and its derivatives: Versatile and sustainable bio-resources for healthcare, *Mater. Sci. Eng., C*, 2020, **113**, 110963, DOI: 10.1016/j.msec.2020.110963.

19 A. Kara, S. Tamburaci, F. Tihminlioglu and H. Havitcioglu, Bioactive fish scale incorporated chitosan biocomposite scaffolds for bone tissue engineering, *Int. J. Biol. Macromol.*, 2019, **130**, 266–279, DOI: 10.1016/j.ijbiomac.2019.02.067.

20 M. Zhu, H. Ye, J. Fang, C. Zhong, J. Yao, J. Park, *et al.*, Engineering High-Resolution Micropatterns Directly onto Titanium with Optimized Contact Guidance to Promote Osteogenic Differentiation and Bone Regeneration, *ACS Appl. Mater. Interfaces*, 2019, **11**(47), 43888–43901, DOI: 10.1021/acsami.9b16050.

21 E. Buck, H. Li and M. Cerruti, Surface Modification Strategies to Improve the Osseointegration of Poly(etheretherketone) and Its Composites, *Macromol. Biosci.*, 2020, **20**(2), e1900271, DOI: 10.1002/mabi.201900271.

22 H. Lee, S. M. Dellatore, W. M. Miller and P. B. Messersmith, Mussel-inspired surface chemistry for multifunctional coatings, *Science*, 2007, **318**(5849), 426–430, DOI: 10.1126/science.1147241.

23 S. P. Gao, D. Zhang, M. Pedrero, Z. M. Guo, J. M. Pingarrón, S. Campuzano, *et al.*, Advances and opportunities of polydopamine coating in biosensing: Preparation, functionality, and applications, *Coord. Chem. Rev.*, 2024, **501**, 215564, DOI: 10.1016/j.ccr.2023.215564.

24 X. Bao, J. Zhao, J. Sun, M. Hu and X. Yang, Polydopamine Nanoparticles as Efficient Scavengers for Reactive Oxygen Species in Periodontal Disease, *ACS Nano*, 2018, **12**(9), 8882–8892, DOI: 10.1021/acsnano.8b04022.

25 J. Li, H. Qiu, H. Gong and W. Tong, Broad-Spectrum Reactive Oxygen Species Scavenging and Activated Macrophage-Targeting Microparticles Ameliorate Inflammatory Bowel Disease, *Biomacromolecules*, 2021, **22**(7), 3107–3118, DOI: 10.1021/acs.biomac.1c00551.

26 W. Ma, X. Zhang, Y. Liu, L. Fan, J. Gan, W. Liu, *et al.*, Polydopamine Decorated Microneedles with Fe-MSC-Derived Nanovesicles Encapsulation for Wound Healing, *Adv. Sci.*, 2022, **9**(13), e2103317, DOI: 10.1002/advs.202103317.

27 Y. Li, L. Yang, Y. Hou, Z. Zhang, M. Chen, M. Wang, *et al.*, Polydopamine-mediated graphene oxide and nanohydroxyapatite-incorporated conductive scaffold with an immunomodulatory ability accelerates periodontal bone regeneration in diabetes, *Bioact. Mater.*, 2022, **18**, 213–227, DOI: 10.1016/j.bioactmat.2022.03.021.

28 Y. L. Cheng, Y. W. Chen, K. Wang and M. Y. Shie, Enhanced adhesion and differentiation of human mesenchymal stem cell inside apatite-mineralized/poly(dopamine)-coated poly(epsilon-caprolactone) scaffolds by stereolithography, *J. Mater. Chem. B*, 2016, **4**(38), 6307–6315, DOI: 10.1039/c6tb01377e.

29 N. G. Rim, S. J. Kim, Y. M. Shin, I. Jun, D. W. Lim, J. H. Park, *et al.*, Mussel-inspired surface modification of poly(L-lactide) electrospun fibers for modulation of osteogenic differentiation of human mesenchymal stem cells, *Colloids Surf., B*, 2012, **91**, 189–197, DOI: 10.1016/j.colsurfb.2011.10.057.

30 S. Su, R. Wang, J. Bai, Z. Chen and F. Zhou, Novel Decellularization Scheme for Preparing Acellular Fish Scale Scaffolds for Bone Tissue Engineering, *ACS Omega*, 2025, **10**(1), 230–238, DOI: 10.1021/acsomega.4c05096.

31 Y. Tang, C. Chen, F. Liu, S. Xie, J. Qu, M. Li, *et al.*, Structure and ingredient-based biomimetic scaffolds combining with autologous bone marrow-derived mesenchymal stem cell sheets for bone-tendon healing, *Biomaterials*, 2020, **241**, 119837, DOI: 10.1016/j.biomaterials.2020.119837.

32 A. Boskey and N. Pleshko Camacho, FT-IR imaging of native and tissue-engineered bone and cartilage, *Biomaterials*, 2007, **28**(15), 2465–2478, DOI: 10.1016/j.biomaterials.2006.11.043.

33 N. T. Khanarian, M. K. Boushell, J. P. Spalazzi, N. Pleshko, A. L. Boskey and H. H. Lu, FTIR-I compositional mapping of the cartilage-to-bone interface as a function of tissue region and age, *J. Bone Miner. Res.*, 2014, **29**(12), 2643–2652, DOI: 10.1002/jbmr.2284.

34 P. M. Crapo, T. W. Gilbert and S. F. Badylak, An overview of tissue and whole organ decellularization processes, *Biomaterials*, 2011, **32**(12), 3233–3243, DOI: 10.1016/j.biomaterials.2011.01.057.

35 S. Dimassi, N. Tabary, F. Chai, C. Zobrist, J. C. Hornez, F. Cazaux, *et al.*, Polydopamine treatment of chitosan nanofibers for the conception of osteoinductive scaffolds for bone reconstruction, *Carbohydr. Polym.*, 2022, **276**, 118774, DOI: 10.1016/j.carbpol.2021.118774.

36 L. Guo, Z. Liang, L. Yang, W. Du, T. Yu, H. Tang, *et al.*, The role of natural polymers in bone tissue engineering, *J. Controlled Release*, 2021, **338**, 571–582, DOI: 10.1016/j.jconrel.2021.08.055.

37 L. Fan, S. Chen, M. Yang, Y. Liu and J. Liu, Metallic Materials for Bone Repair, *Adv. Healthcare Mater.*, 2024, **13**(3), e2302132, DOI: 10.1002/adhm.202302132.

38 D. Khang, J. Lu, C. Yao, K. M. Haberstroh and T. J. Webster, The role of nanometer and sub-micron surface features on vascular and bone cell adhesion on titanium, *Biomaterials*, 2008, **29**(8), 970–983, DOI: 10.1016/j.biomaterials.2007.11.009.

39 H. Jeon, S. Koo, W. M. Reese, P. Loskill, C. P. Grigoropoulos and K. E. Healy, Directing cell migration and organization via nanocrater-patterned cell-repellent interfaces, *Nat. Mater.*, 2015, **14**(9), 918–923, DOI: 10.1038/nmat4342.

40 R. A. Gittens, T. McLachlan, R. Olivares-Navarrete, Y. Cai, S. Berner, R. Tannenbaum, *et al.*, The effects of combined micron-/submicron-scale surface roughness and nanoscale features on cell proliferation and differentiation, *Biomaterials*, 2011, **32**(13), 3395–3403, DOI: 10.1016/j.biomaterials.2011.01.029.

41 X. Lin, B. Kong, Y. Zhu and Y. Zhao, Bioactive Fish Scale Scaffolds with MSCs-Loading for Skin Flap Regeneration, *Adv. Sci.*, 2022, **9**(21), e2201226, DOI: 10.1002/advs.202201226.

42 K. J. Burg, S. Porter and J. F. Kellam, Biomaterial developments for bone tissue engineering, *Biomaterials*, 2000, **21**(23), 2347–2359, DOI: 10.1016/s0142-9612(00)00102-2.

43 Y. Guan, B. Yang, W. Xu, D. Li, S. Wang, Z. Ren, *et al.*, Cell-Derived Extracellular Matrix Materials for Tissue Engineering, *Tissue Eng., Part B*, 2022, **28**(5), 1007–1021, DOI: 10.1089/ten.TEB.2021.0147.

44 C. Xue, L. Chen, N. Wang, H. Chen, W. Xu, Z. Xi, *et al.*, Stimuli-responsive hydrogels for bone tissue engineering, *Biomaterials Translational*, 2024, **5**(3), 257–273, DOI: 10.12336/biomatertransl.2024.03.004.

45 E. A. Zimmermann, B. Gludovatz, E. Schaible, N. K. Dave, W. Yang, M. A. Meyers, *et al.*, Mechanical adaptability of the Bouligand-type structure in natural dermal armour, *Nat. Commun.*, 2013, **4**, 2634, DOI: 10.1038/ncomms3634.

46 D. Arola, S. Murcia, M. Stossel, R. Pahuja, T. Linley, A. Devaraj, *et al.*, The limiting layer of fish scales: Structure and properties, *Acta Biomater.*, 2018, **67**, 319–330, DOI: 10.1016/j.actbio.2017.12.011.

47 Y. S. Lin, C. T. Wei, E. A. Olevsky and M. A. Meyers, Mechanical properties and the laminate structure of Arapaima gigas scales, *J. Mech. Behav. Biomed. Mater.*, 2011, **4**(7), 1145–1156, DOI: 10.1016/j.jmbbm.2011.03.024.

48 Z. Fang, Y. Wang, Q. Feng, A. Kienzle and W. E. Muller, Hierarchical structure and cytocompatibility of fish scales from Carassius auratus, *Mater. Sci. Eng., C*, 2014, **43**, 145–152, DOI: 10.1016/j.msec.2014.07.015.

49 F. Wauquier, L. Leotoing, V. Coxam, J. Guicheux and Y. Wittrant, Oxidative stress in bone remodelling and disease, *Trends Mol. Med.*, 2009, **15**(10), 468–477, DOI: 10.1016/j.molmed.2009.08.004.

50 S. Tan, Y. Wang, Y. Du, Y. Xiao and S. Zhang, Injectable bone cement with magnesium-containing microspheres enhances osteogenesis via anti-inflammatory immunoregulation, *Bioact. Mater.*, 2021, **6**(10), 3411–3423, DOI: 10.1016/j.bioactmat.2021.03.006.

51 P. Zhang, Q. Qin, X. Cao, H. Xiang, D. Feng, D. Wusiman, *et al.*, Hydrogel microspheres for bone regeneration through regulation of the regenerative microenvironment, *Biomaterials Translational*, 2024, **5**(3), 205–235, DOI: 10.12336/biomatertransl.2024.03.002.